PAPER

Check for updates

Structurally tunable plasmonic absorption bands in a self-assembled nano-hole array

Qiang Li, [iD] [a,c] Zizheng Li,*[a] Xiaoyi Wang,[a] Tongtong Wang,[a] Hai Liu,[a] Haigui Yang,[a] Yan Gong[b,c] and Jinsong Gao*[a,c]

In this paper, we demonstrate a theoretical and experimental study on a nano-hole array that can realize perfect absorption in the visible and near-infrared regions. The absorption spectrum can be easily controlled by adjusting the structural parameters including the radius and period of the nano-hole, and the maximal absorption can reach 99.0% in theory. In order to clarify the physical mechanism of the absorber, we start from the extraordinary optical transmission supported by the nano-hole array in a thin metallic film coated on a glass substrate, and then analyse the perfect absorption in the metal–insulator–metal structure. The surface plasmon modes supported by the nano-hole array are completely clarified and both the FDTD simulation and waveguide theory are used to help us understand the physical mechanism, which can provide a new perspective in designing this kind of perfect absorber. In addition, the nano-hole array can be fabricated by simple and low-cost nanosphere lithography, which makes it a more appropriate candidate for spectroscopy, photovoltaics, photodetectors, sensing, and surface enhanced Raman scattering.

1. Introduction

Metallic nanostructures have attracted much attention due to their unique ability of manipulating light–matter interaction at the nanoscale.[1–5] In general, when a beam of incident electromagnetic waves imprints the metal nanostructure, surface plasmons (SPs) can be excited because of the coherent oscillations of free electrons in metals which are categorized into propagating surface plasmon polaritons (SPPs) at the metal-dielectric interface and localized surface plasmons (LSPs) around the metallic nanostructures.[6–8] The excitation of SPs can focus optical energy into the subwavelength region and adjust their spectral response by engineering the shape, size, and material of the structure as well as its dielectric environment. These characteristics make SPs play a vital role in various scientific fields such as biological and chemical sensors,[9–11] plasmonic photocatalysts,[12,13] nonlinear optics,[14,15] surface-enhanced Raman scattering (SERS),[16,17] wave-guiding[18,19] and energy harvesting.[20–28] Energy harvesting devices based on surface plasmons have been widely studied

because of their great scientific values and potential applications. The controllable perfect absorption properties of plasmonic absorbers such as grating,[23] nano-cubes,[24] nano-particles,[25] and nano-cones[27] were investigated both in theory and experiment recently.

Among various kinds of metallic nanostructures, the nano-hole array in a thin metal film has received particular attention since the discovery of the extraordinary optical transmission (EOT) phenomenon by Ebbesen and co-workers in 1998.[29] When the incident electromagnetic wave interacts with the subwavelength hole array patterned in the optical thick metal film, the transmission intensity can be several orders stronger than the prediction of classic Bethe theory. It is generally accepted that the surface plasmon modes propagating on both surfaces of the metal film underlie the physics of the EOT phenomenon.[30–32] In addition to the EOT, many excellent studies have demonstrated the role of the nano-hole array in structural color printing or perfect absorbers.[33–37] These studies generally involve a triple-layer metal–insulator–metal (MIM) structure with the nano-hole array patterned in the top metal layer. SPs can be excited and adjusted by the structural size to realize the desirable spectral characteristic. However, these studies usually focus on the experimental optical properties because of lack of theoretical support. Further investigations in theory are necessary.

In this paper, we used nanosphere lithography and the reactive ion etching (RIE) method to fabricate the nano-hole array in two different structures. Firstly, the EOT phenomenon and

[a]Key Laboratory of Optical System Advanced Manufacturing Technology, Changchun Institute of Optics, Fine Mechanics and Physics, Chinese Academy of Sciences, Changchun 130033, China. E-mail: lizizheng1987@163.com
[b]Jiangsu Key Laboratory of Medical Optics, Suzhou Institute of Biomedical Engineering and Technology, Chinese Academy of Sciences, Suzhou 215163, China
[c]University of the Chinese Academy of Sciences, Beijing 100039, China. E-mail: gaojs999@163.com

its physical origin were analysed. On this basis, perfect absorption of the MIM structure was discussed, in which a rounded analysis of the existing SPs was discussed by the FDTD simulation and waveguide theory. In addition, the nano-hole array in the thin Ag film is fabricated by a controlled nanosphere lithography, which has been widely exploited in the fabrication of nanostructures, possessing advantages of a large area, low cost, and an easy fabrication process.

2. Theory and simulation analysis

First of all, the EOT phenomenon of the nano-hole array patterned in the 100 nm thickness Ag layer on the glass substrate as shown in Fig. 1(a) was investigated. We sweep the radius r of the nano-hole with fixed period P = 550 nm and plot the simulated transmission as a function of r and the incident wavelengths. Two transmission peaks marked as T_1 and T_2 are evident in Fig. 1(b) in which both the locations of transmission peaks T_1 and T_2 almost remain constant with varying r. This is because EOT occurs when the SPP modes are excited and the resonance wavelength of SPPs is just determined by the array period and the angle of incident light independent of the value of r. So we attribute the origin of transmission peaks T_1 and T_2 to the excitation of SPPs by 2D grating coupling. Fig. 1(c) shows the transmission of the 100 nm thickness Ag layer with and without the nano-hole array, in which the two EOT peaks T_1 and T_2 are located at wavelengths of 558.7 nm and 795.4 nm.

In order to clarify the role of SPPs in the mechanism of the EOT phenomenon, we need to calculate the dispersion relations of the 100 nm thickness Ag film without the nano-hole array on the glass substrate. The air, Ag layer, and glass substrate form an insulator–metal–insulator (IMI) configuration as shown in Fig. 1(a) whose dispersion relations of the SPPs propagating at the metal–insulator interface can be calculated directly from the Maxwell equations and its boundary conditions in a planar geometry:[38,39]

$$\left(\frac{\varepsilon_2(w)}{\varepsilon_1(w)} + \frac{\gamma_2(w)}{\gamma_1(w)}\right)\left(\frac{\varepsilon_0}{\varepsilon_1(w)} + \frac{\gamma_0(w)}{\gamma_1(w)}\right)e^{2\gamma_1(w)T}$$
$$= \left(\frac{\varepsilon_2(w)}{\varepsilon_1(w)} - \frac{\gamma_2(w)}{\gamma_1(w)}\right)\left(\frac{\varepsilon_0}{\varepsilon_1(w)} - \frac{\gamma_0(w)}{\gamma_1(w)}\right) \quad (1)$$

$$\gamma_i(w) = k^2 - \varepsilon_i \cdot k_0{}^2 \quad (2)$$

While in a metal film with a periodic hexagonal array of holes, SPPs are excited by grating coupling obeying momentum and energy conservation whose wave vector satisfies the equation below:[40]

$$k_{spp} = k_0 \cdot \sin\theta + \sqrt{\frac{4}{3}(i^2 + i\cdot j + j^2)} \cdot \frac{2\pi}{L} \quad (3)$$

Here, ε_i (i = 0, 1, 2) is the dielectric constant of the air, Ag layer, and glass substrate, respectively. The dielectric constant of the glass substrate we used in calculation ε_2 is 2.25 and T is the thickness of the Ag layer. $k_0 = \omega/c$ is the free-space wave vector and ω is the angular frequency. θ is the angle of the incident wave, i and j are the resonance orders, and P is the
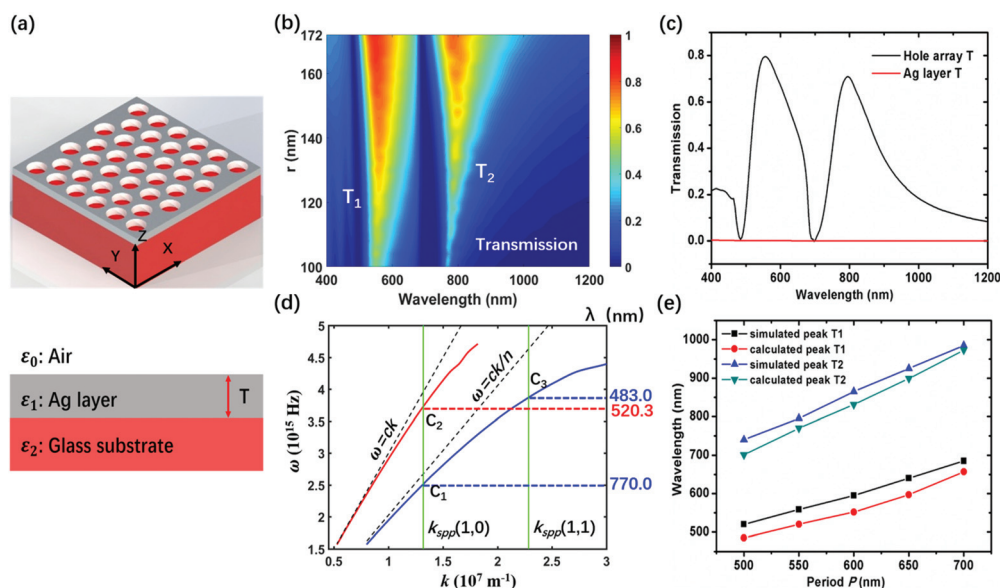

Fig. 1 (a) Schematic of the 100 nm thickness Ag layer with the nano-hole array coated on the glass substrate. Cross-sectional view of the structure. (b) Simulated transmission as a function of wavelength and radius r with fixed period P 550 nm for a 100 nm thickness Ag layer with the nano-hole array coated on the glass substrate. (c) The black line is simulated transmission when r = 160 nm extracted from (b). The red line is the simulated transmission for a 100 nm thickness Ag layer coated on the glass substrate. (d) Dispersion relationship calculated using eqn (1) and (2) for a thin Ag film supported by a glass substrate when T is 100 nm. The two green lines indicated by $k_{spp}(1,0)$ and $k_{spp}(1,1)$ are the wave vector calculated by eqn (3) when the period of the nano-hole array is 550 nm. (e) The relationship between period P and the wavelengths of two EOT peaks obtained by eqn (1)–(3) and FDTD simulation, respectively.

period of the nano-hole array. Only when $k = k_{spp}$ does the energy carried by the incident electromagnetic wave can be transferred to the SPPs propagating at the metal–insulator interface, which is the so-called wave vector matching condition.[30]

The dispersion relationships can be obtained by solving eqn (1)–(3) in the numerical algorithm. The calculated results are shown in Fig. 1(d). For each wave vector k, there are two SPP modes propagating at different interfaces. The red line near the light line for vacuum is the external SPP mode propagating at the air–Ag interface, while the blue line that lies below the light line for glass is the internal SPP mode propagating at the Ag–glass interface. From eqn (3), we can calculate the wavevector of SPP $k_{spp}(1,0) = k_{spp}(0,1) = 1.3191269 \times 10^7$ m^{-1} and $k_{spp}(1,1) = 2.2847947 \times 10^7$ m^{-1} indicated by the green lines for $P = 550$ nm, $\theta = 0$. The three cross points C_1, C_2, and C_3 satisfy the wave vector matching condition $k = k_{spp}$. So the angular frequency ω can be read directly from the left Y-axis ($\omega c_1 = 2.451 \times 10^{15}$ Hz, $\omega c_2 = 3.623 \times 10^{15}$ Hz, and $\omega c_3 = 3.900 \times 10^{15}$ Hz). Finally, the wavelengths of the EOT peaks can be obtained $\lambda_1(1,0) = 770.0$ nm, $\lambda_2(1,0) = 520.3$ nm, and $\lambda_3(1,1) = 483.0$ nm using the equation $\lambda = 2\pi c/\omega$, in which $\lambda_2(1,0)$ and $\lambda_1(1,0)$ correspond to the simulated EOT peaks T_1 (558.7 nm) and T_2 (795.4 nm). After the analysis above, the two different transmission peaks T_1 and T_2 can be assigned to the (1,0) SPP modes at the Ag–air and Ag–glass interfaces, respectively. As shown in the theoretical calculation, there is another EOT peak at a wavelength of 483.0 nm. However, this peak is not obvious in Fig. 1(b) and (c) because the incident light originally passes through the hole when the diameter of the hole has little difference with the wavelength. Therefore, we will not discuss this EOT peak. The wavelengths of EOT peaks T_1 and T_2 for different period P simulated by FDTD and calculated by eqn (1)–(3) are shown in Fig. 1(e), which exhibits a good conformity.

The relative magnetic field $|H|^2$ and relative electric field Re (E_z) distributions at the wavelengths of two transmission peaks T_1 and T_2 are simulated on the X–Z plane when r is 160 nm and P is 550 nm, which can further illustrate the SPP mode. As shown in Fig. 2(a) and (b), the magnetic field intensity is mainly confined at the Ag–air and Ag–glass interfaces, and the decay length into the metal is shorter than that in the dielectric medium, which indicate that the external and internal SPP modes are excited by the incident light coupled with the nano-hole array. One difference is that some incident light can pass through the nano-hole directly in Fig. 2(a) because the wavelength is not much larger than the diameter of the nano-hole. The charge density can be deduced from the Re(E_z) distributions from Fig. 2(c) and (d). At the wavelengths of two transmission peaks T_1 and T_2, the electric field distributions appear antisymmetric and symmetric, which indicate the bonding and antibonding modes.[41]

In the previous section, we have discussed the EOT phenomenon and its physical mechanism. Now we will analyse the perfect absorption in the metal–insulator–metal (MIM) structure which consists of a 150 nm thickness bottom
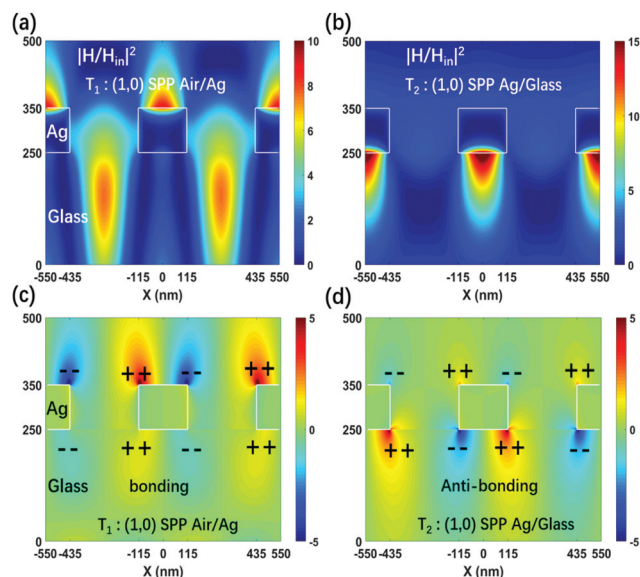

Fig. 2 (a) and (b) The relative magnetic field distributions at the wavelength of transmission peaks T_1 and T_2 on the X–Z plane when r is 160 nm and period P is 550 nm. (c) and (d) The relative electric field E_z and charge distributions at the wavelength of peaks T_1 and T_2 on the X–Z plane when r is 160 nm and period P is 550 nm.

Ag layer, a 50 nm SiO$_2$ layer, and a 100 nm top Ag layer with a patterned nano-hole array as shown in Fig. 3(a). We sweep the radius r of the nano-hole with fixed period $P = 550$ nm and plot the simulated absorption as a function of r and the incident wavelength. It is evident from Fig. 3(b) that three different modes lead to three distinct absorption peaks marked as A_1, A_2, and A_3 in which the location of A_3 strongly depends on the radius r and A_1 and A_2 are a little shifting with varying r. For clarify, the physical mechanism of these absorption peaks and the relative magnetic field $|H|^2$ distributions by FDTD simulation at the cross points of 1 to 4 are shown in Fig. 3(c)–(f). As clearly we can see, the absorption peak A_1 (552.1 nm) and the EOT peak T_1 (558.7 nm) are almost at the same wavelength approximately independent of the value of r, and the magnetic field at point 1 is mainly bound at the air–Ag interface similar to the distributions in the Fig. 2(a), which implies the common origin of the excitation of (1,0) SPP at the air–Ag interface. In Fig. 3(d), the magnetic field at point 2 is mainly confined at the Ag–SiO$_2$ interface indicating the SPP propagating at the Ag–SiO$_2$ interface. In the previous section, we have demonstrated that the wavelength of SPPs is decided by the period P independent of the value of r, but the absorption peaks A_1 and A_2 shift closer to each other, which can be explained by the coupling between the SPP modes at the different interfaces, so the resonance peaks have a little shift. The magnetic field at point 3 in Fig. 3(e) is localized at both the air–Ag and Ag–SiO$_2$ interfaces, which indicates the hybrid mode induced by the coupled SPP at different interfaces, while the magnetic field at point 4 in Fig. 3(f) exhibits a completely different distribution that is confined and enhanced to more than 180 times in the SiO$_2$ gap between the two metal Ag
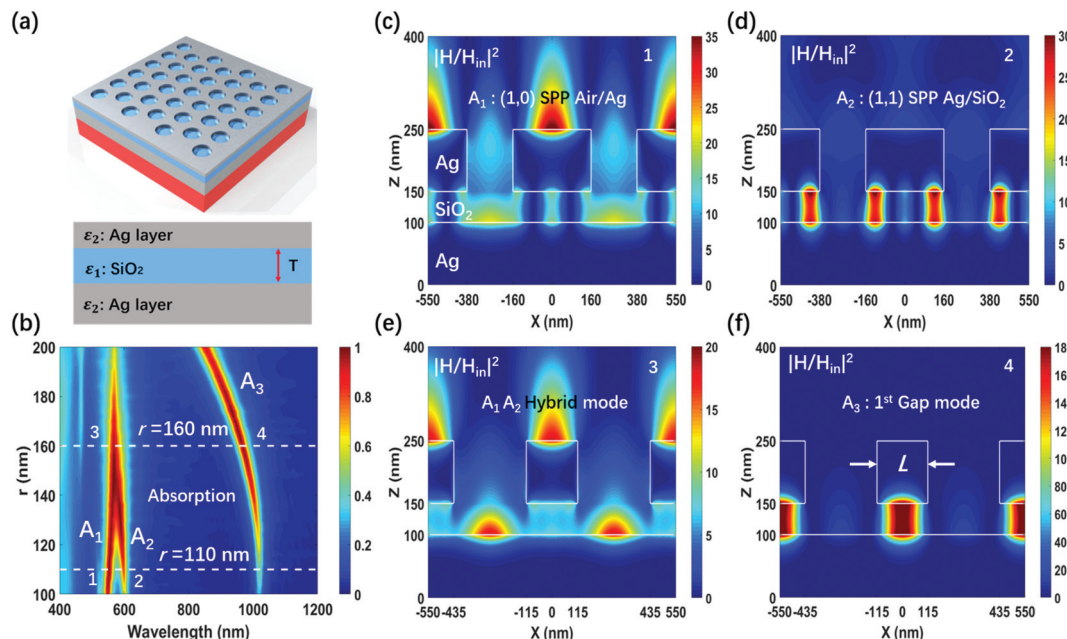
Fig. 3 (a) Schematic of the triple-layer MIM structure consisting of a periodic nano-hole array patterned in a 100 nm Ag layer, thin SiO$_2$ layer, and 150 nm Ag layer. Cross-sectional view of the structure. (b) Simulated absorption for the MIM structure as a function of wavelength and the radius of the hole r with fixed period P = 550 nm. The two white dashed lines indicate the locations of r = 110 nm and r = 160 nm. The numbers 1 to 4 indicate the cross points of the dash lines and absorption peaks A_1, A_2, and A_3. (c) and (d) The relative magnetic field distributions at the wavelengths of peaks A_1 and A_2 on the X–Z plane when r is 110 nm and period P is 550 nm. (e) and (f) The relative magnetic field distributions at the wavelength of hybrid and A_3 modes on the X–Z plane when r is 160 nm and period P is 550 nm.

layers, which are the distinct characters for the gap plasmon (GP) mode. There is one antinode in the gap indicating that the first order of standing wave resonance is excited by surface plasmon. Note that for the symmetry reason only odd modes (m = 1, 3, 5...) can be excited in the considered MIM structure for the normal incident light. Here, we introduce the length L of the Ag layer between two adjacent holes as shown in Fig. 3(f). The value of the L is a key factor for the excitation of the GP mode, which we will discuss later. It should be noted that we attribute the A_2 mode to the SPP propagating at the Ag–SiO$_2$ interface rather than the third order GP mode, because in Fig. 3(d) the magnetic field is mainly confined at the Ag–SiO$_2$ interface different from the distribution in Fig. 3(f), in which the most energy is localized in the SiO$_2$ gap. Meanwhile, there are just two red regions in the gap, but in the third order GP mode there must be three red regions.

In addition, we also use eqn (1) and (2) to calculate the dispersion relationships of two Ag thin films spaced by a SiO$_2$ layer as shown in Fig. 3(a). In this situation, the ε_i (i = 0, 1, 2) is the dielectric constant of Ag, SiO$_2$, and Ag, respectively. The dispersion curves, ω (frequency) versus k, for different values of the SiO$_2$ thickness (T) are plotted in Fig. 4(a). The k_{spp} calculated by eqn (3) is indicated by the grey dashed line and their cross points are the wave vector of SPPs, from which we can obtain the $\lambda_{A_2}(1,1)$ = 602.1 nm for T = 50 nm according to the location of the absorption peak A_2 (601.0 nm). For the absorption peak A_3, it is well known that the resonant modes in the
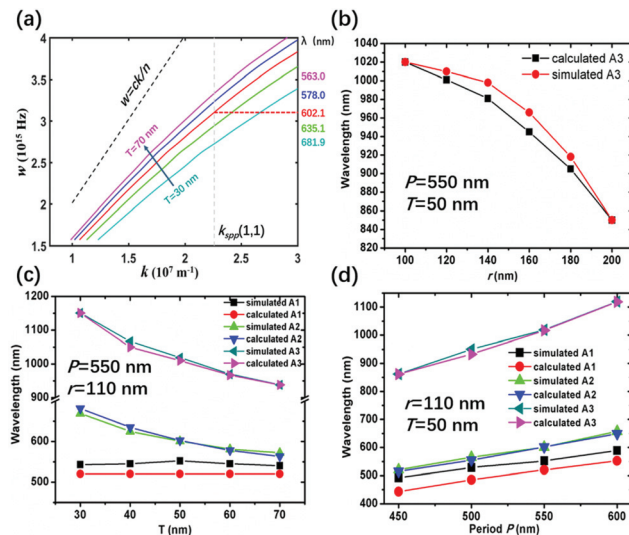

Fig. 4 (a) Dispersion relationships of the MIM structure calculated using eqn (1) and (2) for different SiO$_2$ film thicknesses: T = 30 nm, 40 nm, 50 nm, 60 nm, and 70 nm. The grey dashed line indicated by $k_{spp}(1,1)$ is the wave vector calculated by eqn (3) when the period of the nano-hole array is 550 nm. (b) The relationship between the radius r and the wavelengths of absorption peak A_3 (P = 550 nm, T = 50 nm) obtained by eqn (1)–(4) and FDTD simulation, respectively. (c) The relationship between the absorption peak wavelengths and SiO$_2$ film thickness T when P = 550 nm, r = 110 nm. (d) The relationship between absorption peak wavelengths and period P when T = 50 nm and r = 110 nm. The simulated and calculated results obtained by FDTD and eqn (1)–(4), respectively.

gap are formed by the interference of forward and backward propagating waves and are determined by:[42,43]

$$2Lk + \Delta\phi = 2m\pi \qquad (4)$$

where k is the wave vector of the propagating surface plasmon in the waveguide, L is the length of the gap indicated in Fig. 3(f), $\Delta\phi$ is the phase change at the two ends of the boundary, and m is the resonant order. Here, $m = 1$, $L = P - 2r$, $\Delta\phi$ can be estimated as shown in the description in ref. 42–45. Therefore, the k can be obtained from eqn (4), and the angular frequency ω can be read directly from the left Y-axis in Fig. 4(a), and then the wavelength λ can be obtained by $\lambda = 2\pi c/\omega$. The calculated resonant wavelengths of peak A_3 for different values of r when period P is 550 nm are according to the simulated results by FDTD in Fig. 4(b). In the same way, the relationship of absorption peaks and the SiO_2 thickness (T) is shown in Fig. 4(c), in which the A_1 mode is almost not shifting for different T because of the excitation of the SPP at the air–Ag interface. The calculated wavelengths of A_2 and A_3 modes for different T fit well with the simulated results by FDTD. Similarly, the relationship of absorption peaks and the period (P) is also given in Fig. 4(d). All of the results calculated in theory and simulated by FDTD coincide well with each other, demonstrating the rationality and validity of our theory. The waveguide theory and FDTD simulation used here can provide a new perspective in designing this kind of absorber.

3.   Experimental validation

The nano-hole array is fabricated by the self-assembled nanosphere lithography, whose fabrication process is shown in Fig. 5. The glass substrate was coated by a 150 nm thick Ag film and a 50 nm thick SiO_2 film in sequence. A close packed PS nanosphere monolayer was prepared by the interface

method.[46–48] The size of the PS spheres was reduced by oxygen plasma using reactive ion etching (RIE) in a controlled manner. Afterward, a 100 nm thick Ag layer was deposited vertically on the non-close packed PS sphere mask. Finally, we removed the PS nanosphere using ultrasonic cleaning in toluene solution for 10 minutes, leading to the formation of the nanohole array in the top Ag layer.

In this fabrication process, the period can be adjusted by the diameter of the PS nanosphere; the diameter of the nanoholes can be controlled by different etching times of the RIE procedure. Fig. 6(a) shows the top-view scanning electron microscopy (SEM) images of the PS sphere monolayer on a large area with a magnified view. Fig. 6(b) shows the PS mono-
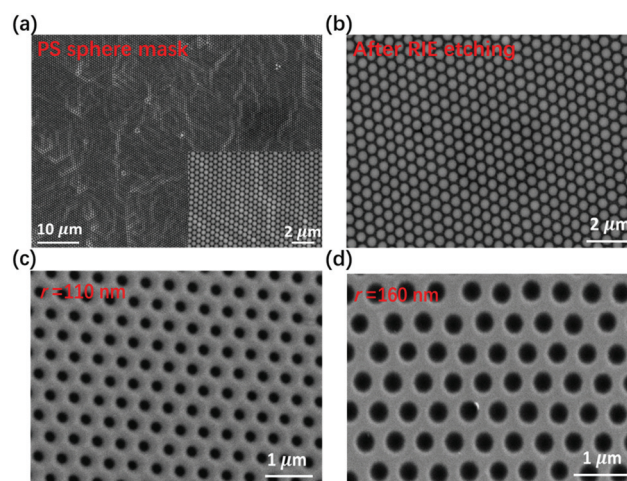

Fig. 6 (a) A large area of the close packed PS monolayer template on the glass substrate with a magnified view. (b) Non-closed PS sphere monolayer after oxygen plasma etching. (c) and (d) The top view of two selected MIM samples with the same period 550 nm and different radius r (110 nm and 160 nm).
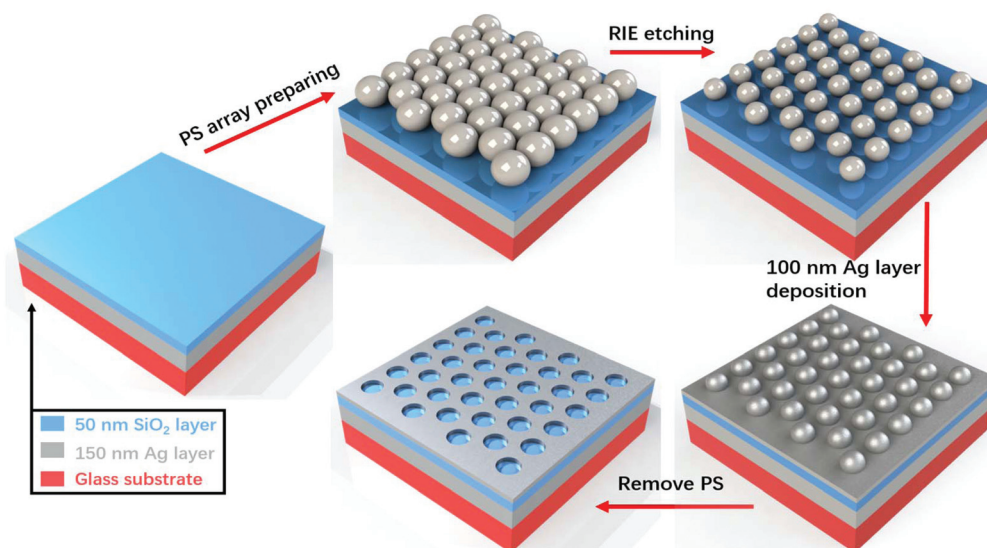

Fig. 5 Fabrication process flow of the nano-hole array in the metal Ag layer.
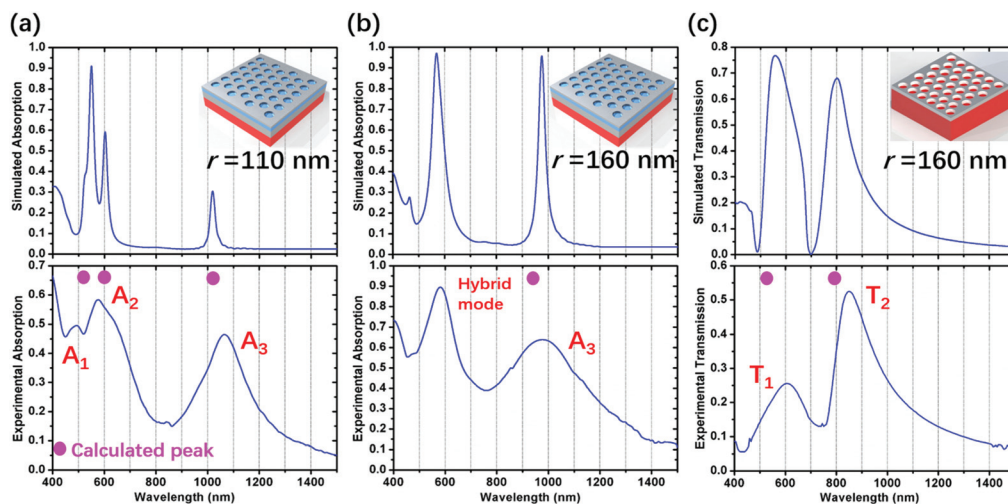
Fig. 7 (a) and (b) Simulated and experimental absorption of the MIM structure with the same period P = 550 nm, different r 110 nm and 160 nm. (c) Simulated and experimental transmission for the 100 nm thickness Ag layer with the nano-hole array coated on a glass substrate. The period P = 550 nm and r = 160 nm. The pink dots are the calculated resonance wavelengths by eqn (1)–(4).

layer after etching. And Fig. 6(c) and (d) show two selected samples with the same period (P = 550 nm) and different hole radii (r = 110 nm and 160 nm), in which the nano-hole array is in a hexagonal lattice displaying a high-quality order.

The experimental results are shown in Fig. 7. When r is 110 nm, there are three absorption peaks indicated as A_1, A_2, and A_3 which can be attributed to the SPP at the air–Ag, Ag–SiO_2 interfaces, and the first order gap mode, respectively. On increasing r to the value of 160 nm, the A_1 and A_2 absorption peaks overlap with each other, forming one single hybrid mode absorption peak at a resonance wavelength of 582 nm. And the A_3 absorption peak is blue shifted obviously. The simulated and experimental transmissions are also given in Fig. 7(c). The pink dots are the calculated wavelengths of the peaks, from which we can see that the results obtained by FDTD simulation, experimental measurement, and theoretical calculation exhibit good agreement. It should be noted that the nano-hole fabricated by the nanosphere lithography is not a standard cylinder and also the permittivity of Ag and SiO_2 used in simulation is different from the experiment, which result in some deviation between the experimental and simulated results. But the peaks can be measured in the experiment according to the simulation, which still demonstrate the simulated analysis and theoretical calculation in the previous section.

4. Conclusions

In conclusion, we have successfully demonstrated a MIM perfect absorber based on surface plasmons in the visible and infrared spectra. The surface plasmon modes including SPP, GP, and hybrid modes supported by the nanohole array were thoroughly clarified by both FDTD simulation and waveguide theory, which can be used to design this kind of perfect absor-

ber. The simulated, calculated, and experimental results fit each other well which further demonstrates the correctness. In addition, the proposed absorber can be fabricated by a low-cost nanosphere lithography, which makes it a more appropriate candidate for many applications such as photovoltaics, spectroscopy, sensing, and photodetectors.

5. Simulation model

The 3D finite-difference time-domain (FDTD) simulation is performed using commercial software (Lumerical FDTD Solutions) to investigate the optical properties of the proposed structure, where the periodic boundary conditions are adopted for a unit cell in both X and Y directions and perfectly matched layers (PML) are applied in the Z direction. The permittivity of Ag and SiO_2 used in simulation is extracted from the data of Palik.[49] A discrete mesh with the size of $2 \times 2 \times 1$ nm^3 is used for the top Ag layer. The thickness of the bottom Ag layer is set to be 150 nm which is several times larger than the skin depth so that the incident light transmission through the structure can be completely inhibited. Therefore, the absorption is $A = 1 - R$ where R is the reflection. The incident source is a linearly polarized plane wave (400 nm–1200 nm) propagating along the negative Z direction with the E field polarization to the X direction.

6. Experimental section

Before making the PS sphere mask, the K9 glass substrate was ultrasonically cleaned in acetone, ethanol, and distilled water for 30 min. The purchased PS spheres (550 nm in diameter) in an aqueous solution (10 wt%) were mixed with an equal volume of ethanol. A close packed PS nanosphere monolayer

was prepared by the interface method.[46–48] The size of the PS sphere mask was reduced by the RIE technique using oxygen gas (5 sccm, 30 mTorr pressure, RF power 250 W, Trion, Phantom III RIE). The Ag layer was deposited by DC reactive magnetron sputtering at a rate of 4.28 A s^{-1} with 150 W power, 1.0 Pa pressure, while the SiO_2 layer was deposited by the method of RF reactive magnetron sputtering at a rate of 0.63 A s^{-1} with 80 W power and 1.0 Pa pressure. The experimental reflection (R) and transmission (T) are measured using a spectrometer (PerkinElmer Lambda-1050) equipped with a 160 mm integrating sphere. The experimental absorption (A) is calculated by subtracting the sum of normalized reflection and transmission from unity.

Conflicts of interest

There are no conflicts to declare.

Acknowledgements

Notes and references

1 C. F. Guo, T. Y. Sun, F. Cao, Q. Liu and Z. F. Ren, *Light: Sci. Appl.*, 2014, **3**, e161.

2 H. Chalabi, D. Schoen and M. L. Brongersma, *Nano Lett.*, 2014, **14**, 1374.

3 R. Ameling, D. Dregely and H. Giessen, *Opt. Lett.*, 2011, **36**, 2218.

4 Q. Li, J. Gao, H. Yang, H. Liu, X. Wang, Z. Li and X. Guo, *Plasmonics*, 2017, **12**, 1037.

5 Z. Yong, S. Zhang, C. Gong and S. He, *Sci. Rep.*, 2016, **6**, 24063.

6 Y. Z. Chu, M. G. Banaee and K. B. Crozier, *ACS Nano*, 2010, **4**, 2804.

7 J. Chen, P. Wang, Z. M. Zhang, Y. Lu and H. Ming, *Phys. Rev. E: Stat., Nonlinear, Soft Matter Phys.*, 2011, **84**, 026603.

8 Y. Chu and K. B. Crozier, *Opt. Lett.*, 2009, **34**, 244.

9 S. Liu, X. Qi, W. Zhai, Z. Chen, W. Wang and J. Han, *Nanoscale*, 2015, **7**, 20171.

10 T. Allsop, R. Arif, R. Neal, K. Kalli, V. Kundrat, A. Rozhin, P. Culverhouse and D. J. Webb, *Light: Sci. Appl.*, 2016, **5**, e16036.

11 B. Park, S. H. Yun, C. Y. Cho, Y. C. Kim, J. C. Shin, H. G. Jeon, Y. H. Huh, I. Hwang, K. Y. Baik, Y. I. Lee, H. S. Uhm, G. S. Cho and E. H. Choi, *Light: Sci. Appl.*, 2014, **3**, e222.

12 C. An, S. Peng and Y. Sun, *Adv. Mater.*, 2010, **22**, 2570–2574.

13 F. Pincella1, K. Isozaki and K. Miki, *Light: Sci. Appl.*, 2014, **3**, e133.

14 M. A. Foster, A. C. Turner, M. Lipson and A. L. Gaeta, *Opt. Express*, 2008, **16**, 1300.

15 P. Genevet, J. Tetienne, E. Gatzogiannis, R. Blanchard, M. A. Kats, M. Scully and F. Capasso, *Nano Lett.*, 2010, **10**, 4880.

16 P. Zheng, M. Li, R. Jurevic, S. K. Cushing, Y. Liu and N. Wu, *Nanoscale*, 2015, **7**, 11005.

17 P. Zheng, S. K. Cushing, S. Suria and N. Wu, *Phys. Chem. Chem. Phys.*, 2015, **17**, 21211.

18 R. F. Oulton, V. J. Sorger, D. A. Genov, D. F. P. Pile and X. Zhang, *Nat. Photonics*, 2008, **2**, 496–500.

19 L. Gao, L. Tang, F. Hu, R. Guo, X. Wang and Z. Zhou, *Opt. Express*, 2012, **20**, 11487.

20 C. M. Watts, X. L. Liu and W. J. Padilla, *Adv. Mater.*, 2012, **24**, 98–120.

21 Y. Qu, Q. Li, H. Gong, K. Du, S. Bai, D. Zhao, H. Ye and M. Qiu, *Adv. Opt. Mater.*, 2016, **4**, 480–486.

22 J. Lu, S. Nam, K. Wilke, A. Raza, Y. E. Lee, A. AlGhaferi, N. X. Fang and T. Zhang, *Adv. Opt. Mater.*, 2016, **4**, 1255–1264.

23 B. Y. Zheng, Y. Wang, P. Nordlander and N. J. Halas, *Adv. Mater.*, 2014, **26**, 6318–6323.

24 T. Cao, C. W. Wei, R. E. Simpson, L. Zhang and M. J. Cryan, *Sci. Rep.*, 2014, **4**, 3955.

25 Y. H. Su, Y. F. Ke, S. L. Cai and Q. Y. Yao, *Light: Sci. Appl.*, 2012, **1**, e14.

26 K. Liu, X. Zeng, S. Jiang, D. Ji, H. Song, N. Zhang and Q. Gan, *Nanoscale*, 2014, **6**, 5599.

27 Q. Li, J. Gao, Z. Li, H. Yang, H. Liu, X. Wang and Y. Li, *Opt. Mater.*, 2017, **70**, 165–170.

28 Q. Li, J. Gao, H. Yang and H. Liu, *Plasmonics*, 2016, **11**, 1067–1072.

29 T. W. Ebbesen, H. J. Lezec, H. F. Ghaemi, T. Thio and P. A. Wolff, *Nature*, 1998, **391**, 667–669.

30 C. Genet and T. W. Ebbesen, *Nature*, 2007, **445**, 39–46.

31 H. F. Ghaemi, T. Thio and D. E. Grupp, *Phys. Rev. B: Condens. Matter Mater. Phys.*, 1998, **58**, 6779.

32 W. Yue, Z. Wang, Y. Yang, J. Li, Y. Wu, L. Chen, B. Ooi, X. Wang and X. Zhang, *Nanoscale*, 2014, **6**, 7917.

33 F. Cheng, X. D. Yang, D. Rosenmann, L. Stan, D. Czaplewski and J. Gao, *Opt. Express*, 2015, **23**, 25329.

34 F. Cheng, J. Gao, L. Stan, D. Rosenmann, D. Czaplewski and X. D. Yang, *Opt. Express*, 2015, **23**, 14552.

35 F. Cheng, J. Gao, T. S. Luk and X. Yang, *Sci. Rep.*, 2015, **5**, 11045.

36 B. Debbrecht, M. Mcelhiney, V. Carey, M. S. Mirotznik and B. G. Delacy, *Opt. Express*, 2017, **25**, 24501–24511.

37 X. Zhang, S. Ye, X. Zhang, Z. Li, S. Wu, J. Zhang, T. Wang and B. Yang, *J. Mater. Chem. C*, 2013, **1**, 933.

38 T. Park, N. Mirin, J. B. Lassiter, C. L. Neh, N. J. Halas and P. Nordlander, *ACS Nano*, 2008, **2**, 25–32.

39 J. J. Burke and G. I. Stegeman, *Phys. Rev. B: Condens. Matter Mater. Phys.*, 1986, **33**, 5186.

40 R. Ortuño, C. García-Meca, F. J. Rodríguez-Fortuño, J. Martí and A. Martínez, *Phys. Rev. B: Condens. Matter Mater. Phys.*, 2009, **79**, 075425.

41 T. Rindzevicius, Y. Alaverdyan, B. Sepulveda, T. Pakizeh and M. Ka, *J. Phys. Chem. C*, 2007, **111**, 1207–1212.

42 Y. Huang, X. Zhang, J. Li, L. Mab and Z. Zhang, *J. Mater. Chem. C*, 2017, **5**, 6079.

43 S. I. Bozhevolnyi and T. Søndergaard, *Opt. Express*, 2007, **15**, 10869–10877.

44 E. S. Barnard, J. S. White, A. Chandran and M. L. Brongersma, *Opt. Express*, 2008, **16**, 16529–16537.

45 F. Hu, H. Yi and Z. Zhou, *Opt. Express*, 2011, **19**, 4848–4855.

46 J. Yu, Q. F. Yan and D. Z. Shen, *ACS Appl. Mater. Interfaces*, 2010, **2**, 1922–1926.

47 S. H. Lee, K. C. Bantz, N. C. Lindquist, S. H. Oh and C. L. Haynes, *Langmuir*, 2009, **25**, 13685–13693.

48 M. Pisco, F. Galeotti, G. Quero, G. Grisci, A. Micco, L. V. Mercaldo, P. D. Veneri, A. Cutolo and A. Cusano, *Light: Sci. Appl.*, 2017, **6**, e16229.

49 E. D. Palik, *Handbook of Optical Constants of Solids*, Academic Press, 1985.